

Low-power continuous-wave generation of visible harmonics in silicon photonic crystal nanocavities

Matteo Galli,^{1,*} Dario Gerace,¹ Karl Welna,² Thomas F. Krauss,² Liam O’Faolain,² Giorgio Guizzetti,¹ and Lucio Claudio Andreani¹

¹Dipartimento di Fisica “A. Volta,” Università degli Studi di Pavia, 27100 Pavia, Italy

²School of Physics and Astronomy, University of St. Andrews, Fife KY16 9SS, UK

*matteo.galli@unipv.it

Abstract: We present the first demonstration of frequency conversion by simultaneous second- and third-harmonic generation in a silicon photonic crystal nanocavity using continuous-wave optical excitation. We observe a bright dual wavelength emission in the blue/green (450–525 nm) and red (675–790 nm) visible windows with pump powers as low as few microwatts in the telecom bands, with conversion efficiencies of $\sim 10^{-5}/W$ and $\sim 10/W^2$ for the second- and third-harmonic, respectively. Scaling behaviors as a function of pump power and cavity quality-factor are demonstrated for both second- and third order processes. Successful comparison of measured and calculated emission patterns indicates that third-harmonic is a bulk effect while second-harmonic is a surface-related effect at the sidewall holes boundaries. Our results are promising for obtaining practical low-power, continuous-wave and widely tunable multiple harmonic generation on a silicon chip.

© 2010 Optical Society of America

OCIS codes: (230.5298) Photonic crystals; (230.5750) Resonators; (190.2620) Harmonic generation and mixing.

References and links

1. K. J. Vahala, “Optical microcavities,” *Nature* **424**, 839–846 (2003).
2. R. Salem, M. A. Foster, A. C. Turner, D. F. Geraghty, M. Lipson, and A. L. Gaeta, “Signal regeneration using low-power four-wave mixing on a silicon chip,” *Nat. Photonics* **2**, 35–38 (2007).
3. A. C. Turner, M. A. Foster, A. L. Gaeta, and M. Lipson, “Ultra-low power parametric frequency conversion in a silicon microring resonator,” *Opt. Express* **16**, 4881–4887 (2008).
4. H. Rong, S. Xu, Y.-H. Kuo, V. Sih, O. Cohen, O. Raday, and M. Paniccia, “Low-threshold continuous-wave Raman silicon laser,” *Nat. Photonics* **1**, 232–237 (2007).
5. T. Carmon and K. J. Vahala, “Visible continuous emission from a silica microphotonic device by third-harmonic generation,” *Nat. Phys.* **3**, 430–435 (2007).
6. Y. R. Shen, *The Principles of Nonlinear Optics* (Wiley, New York, 1984).
7. R. Boyd, *Nonlinear Optics* (Academic Press, California, 1992).
8. M. A. Foster, A. C. Turner, J. E. Sharping, B. S. Schmidt, M. Lipson, and A. L. Gaeta, “Broad-band optical parametric gain on a silicon photonic chip,” *Nature* **441**, 960–963 (2006).
9. T. J. Kippenberg, S. M. Spillane, and K. J. Vahala, “Kerr-nonlinearity optical parametric oscillation in an ultrahigh-Q toroid microcavity,” *Phys. Rev. Lett.* **93**, 083904 (2004).
10. O. Boyraz, T. Indukuri, and B. Jalali, “Self-phase-modulation induced spectral broadening in silicon waveguides,” *Opt. Express* **12**, 829–834 (2004).
11. A. R. Cowan, G. W. Rieger, and J. F. Young, “Nonlinear transmission of 1.5 μm pulses through single-mode silicon-on-insulator waveguide structures,” *Opt. Express* **12**, 1611–1621 (2004).

12. E. Dulkeith, Y. A. Vlasov, X. Chen, N. C. Panoiu, and R. M. Osgood Jr. "Self-phase-modulation in submicron silicon-on-insulator photonic wires," *Opt. Express* **14**, 5524–5534 (2006).
13. S. M. Spillane, T. J. Kippenberg, and K. J. Vahala, "Ultra-low threshold Raman laser using a spherical dielectric microcavity," *Nature* **415**, 621–623 (2002).
14. A. Liu, H. Rong, O. Cohen, M. Paniccia, and D. Hak, "Net optical gain in low-loss silicon-on-insulator waveguide by stimulated Raman scattering," *Opt. Express* **112**, 4261–4267 (2004).
15. H. Rong, R. Jones, A. Liu, O. Cohen, D. Hak, A. Fang, and M. Paniccia, "A continuous-wave Raman silicon laser," *Nature* **433**, 725–728 (2005).
16. B. Corcoran, C. Monat, C. Grillet, D. J. Moss, B. J. Eggleton, T. P. White, L. O'Faolain, and T. F. Krauss, "Green light emission in silicon through slow-light enhanced third-harmonic generation in photonic-crystal waveguides," *Nat. Photonics* **3**, 206–209 (2009).
17. M. Notomi, K. Yamada, A. Shinya, J. Takahashi, C. Takahashi, and I. Yokohama, "Extremely large group-velocity dispersion of line-defect waveguides in silicon photonic crystal slabs," *Phys. Rev. Lett.* **87**, 253902 (2001).
18. W. Bogaerts, R. Baets, P. Dumon, V. Wiaux, S. Beckx, D. Taillaert, B. Luyssaert, J. Van Campenhout, P. Bienstman, and D. Van Thourhout, "Nanophotonic waveguides in silicon-on-insulator fabricated with CMOS technology," *J. Lightwave Technol.* **23**, 401–412 (2006).
19. L. O'Faolain, X. Yuan, D. McIntyre, S. Thoms, H. Chong, R. M. De La Rue and T. F. Krauss, "Low-loss propagation in photonic crystal waveguides," *Electron. Lett.* **42**, 1454–1455 (2006).
20. Y. Akahane, T. Asano, B. S. Song, and S. Noda, "High-Q photonic nanocavity in a two-dimensional photonic crystal," *Nature* **425**, 944–947 (2003).
21. B. S. Song, S. Noda, T. Asano, and Y. Akahane, "Ultra-high-Q photonic doubleheterostructure nanocavity," *Nat. Mater.* **4**, 207–210 (2005).
22. T. F. Krauss, "Slow light in photonic crystal waveguides," *J. Phys. D* **40**, 2666–2670 (2007).
23. T. Baba, "Slow light in photonic crystals," *Nat. Photonics* **2**, 465–473 (2008).
24. J. Bravo-Abad, A. Rodriguez, P. Bermel, S. G. Johnson, J. D. Joannopoulos, and M. Soljacic, "Enhanced nonlinear optics in photonic-crystal microcavities," *Opt. Express* **15**, 16161–16176 (2007).
25. M. W. McCutcheon, J. F. Young, G. W. Rieger, D. Dalacu, S. Fr  d  rick, P. J. Poole, and R. L. Williams, "Experimental demonstration of second-order processes in photonic crystal microcavities at submilliwatt excitation powers," *Phys. Rev. B* **76**, 245104 (2007).
26. D. Coquillat, G. Vecchi, C. Comaschi, A. M. Malvezzi, J. Torres, and M. Le Vassor d'Yerville, "Enhanced second- and third-harmonic generation and induced photoluminescence in a two-dimensional GaN photonic crystal," *Appl. Phys. Lett.* **87**, 101106 (2005).
27. S. Combri  , A. De Rossi, Q. V. Tran, and H. Benisty, "GaAs photonic crystal cavity with ultra-high Q: microwatt nonlinearity at 1.55 μm ," *Opt. Lett.* **33**, 1908–1910 (2008).
28. K. Rivoire, Z. Lin, F. Hatami, W. T. Masselink, and J. Vu  kovi  , "Second-harmonic generation in gallium phosphide photonic crystal nanocavities with ultralow continuous wave pump power," *Opt. Express* **17**, 22609–22615 (2009).
29. M. Falasconi, L. C. Andreani, A. M. Malvezzi, M. Patrini, V. Mulloni, and L. Pavesi, "Bulk and surface contributions to second-order susceptibility in crystalline and porous silicon by second-harmonic generation," *Surf. Science* **481**, 105–112 (2001).
30. T. V. Dolgova, A. I. Maidykovski, M. G. Martemyanov, A. A. Fedyanin, O. A. Aktsipetrov, G. Marowsky, V. A. Yakovlev, and G. Mattei, "Giant microcavity enhancement of second-harmonic generation in all-silicon photonic crystals," *Appl. Phys. Lett.* **81**, 2725 (2002).
31. P. P. Markowicz, H. Tiryaki, H. Pudavar, P. N. Prasad, N. N. Lepeshkin, and R. W. Boyd, "Dramatic enhancement of third-harmonic generation in three dimensional photonic crystals," *Phys. Rev. Lett.* **92**, 083903 (2004).
32. M. G. Martemyanov, E. M. Kim, T. V. Dolgova, A. A. Fedyanin, and O. A. Aktsipetrov, "Third-harmonic generation in silicon photonic crystals and microcavities," *Phys. Rev. B* **70**, 073311 (2004).
33. C. Comaschi, G. Vecchi, A. M. Malvezzi, M. Patrini, G. Guizzetti, M. Liscidini, L. C. Andreani, D. Peyrade, and Y. Chen, "Enhanced third-harmonic reflection and diffraction in silicon-on-insulator photonic waveguides," *Appl. Phys. B* **81**, 305–311 (2005).
34. N. Bloembergen, R. K. Chang, S. S. Jha, and C. H. Lee, "Optical second-harmonic generation in reflection from media with inversion symmetry," *Phys. Rev.* **174**, 813 (1968).
35. J. A. Litwin, J. E. Sipe, and H. M. van Driel, "Picosecond and nanosecond second-harmonic generation from centrosymmetric semiconductors," *Phys. Rev. B* **31**, 5543 (1985).
36. P. Guyot-Sionnest, W. Chen, and Y. R. Shen, "General considerations on optical second-harmonic generation from surfaces and interfaces," *Phys. Rev. B* **33**, 8254 (1986).
37. J. E. Sipe, D. J. Moss, and H. M. van Driel, "Phenomenological theory of optical second- and third-harmonic generation from cubic centrosymmetric crystals," *Phys. Rev. B* **35**, 1129 (1987).
38. R. Jones, H. Rong, A. Liu, A. W. Fang, and M. J. Paniccia, "Net continuous wave optical gain in a low loss silicon-on-insulator waveguide by stimulated Raman scattering," *Opt. Express* **13**, 519–525 (2005).
39. T. Tanabe, M. Notomi, S. Mitsugi, A. Shinya, and E. Kuramochi, "All-optical switches on a silicon chip realized

- using photonic crystal nanocavities,” *Appl. Phys. Lett.* **87**, 151112 (2005).
40. A. Witvrouw, B. Du Bois, P. De Moor, A. Verbist, C. Van Hoof, H. Bender, and K. Baert, “A comparison between wet HF etching and vapor HF etching for sacrificial oxide removal,” *Proc. SPIE* **4174** 130–141 (2000).
 41. N.-V.-Q. Tran, S. Combr e, and A. De Rossi, “Directive emission from high-Q photonic crystal cavities through band folding,” *Phys. Rev. B* **79**, 041101 (2009).
 42. M. Toishi, D. Englund, A. Faraon, and J. Vučkovi c, “High-brightness single photon source from a quantum dot in a directional emission nanocavity,” *Opt. Express* **17**, 14618–14626 (2009).
 43. S. L. Portalupi, M. Galli, C. Reardon, T. F. Krauss, L. O’Faolain, L. C. Andreani, and D. Gerace, “Planar photonic crystal cavities with far-field optimization for high coupling efficiency and quality factor,” *Opt. Express* **18**, 16064–16073 (2010).
 44. The 3D FDTD simulations shown in this work have been performed with commercial software from Lumerical Solutions Inc.
 45. L. C. Andreani, D. Gerace, and M. Agio, “Gap maps, diffraction losses, and exciton-polaritons in photonic crystal slabs,” *Photon. Nanostruct. Fundam. Appl.* **2**, 103–110 (2004).
 46. D. Gerace and L. C. Andreani, “Effects of disorder on propagation losses and cavity Q-factors in photonic crystal slabs,” *Photon. Nanostruct. Fundam. Appl.* **3**, 120–128 (2005).
 47. M. McCutcheon, G. W. Rieger, I. W. Cheung, J. F. Young, D. Dalacu, S. Fr ed eric, P. J. Poole, G. C. Aers, and R. Williams, “Resonant scattering and second-harmonic spectroscopy of planar photonic crystal microcavities,” *Appl. Phys. Lett.* **87**, 221110 (2009).
 48. M. Galli, S. L. Portalupi, M. Belotti, L. C. Andreani, L. O’Faolain, and T. F. Krauss, “Light scattering and Fano resonances in high-Q photonic crystal nanocavities,” *Appl. Phys. Lett.* **94**, 071101 (2009).
 49. M. Notomi, A. Shinya, S. Mitsugi, G. Kira, E. Kuramochi, and T. Tanabe, “Optical bistable switching action of Si high-Q photonic-crystal nanocavities,” *Opt. Express* **13**, 2678–2687 (2005).
 50. T. Uesugi, B. S. Song, T. Asano, and S. Noda, “Investigation of optical nonlinearities in an ultra-high-Q Si nanocavity in a two-dimensional photonic crystal slab,” *Opt. Express* **14**, 377–386 (2006).
 51. M. P. Nezhad, A. Simic, O. Bondarenko, B. Slutsky, A. Mizrahi, L. Feng, V. Lomakin, and Y. Fainman, “Room-temperature subwavelength metallo-dielectric lasers,” *Nat. Photonics* **4**, 395–399 (2010).
 52. T. Tanabe, K. Nishiguchi, A. Shinya, E. Kuramochi, H. Inokawa, M. Notomi, K. Yamada, T. Tsuchizawa, T. Watanabe, H. Fukuda, H. Shinjima, and S. Itabashi, “Fast all-optical switching using ion-implanted silicon photonic crystal nanocavities,” *Appl. Phys. Lett.* **90**, 031115 (2007).
-

1. Introduction

Integrated optical micro- and nano-cavities [1], where light is tightly confined in spatial regions just a few wavelengths across, offer a unique way to enhance nonlinear optical processes, enabling a wealth of all-optical functions on a chip scale using low-power light [2–5]. Frequency conversion by nonlinear harmonic generation [6, 7] is a crucial functionality, as it allows the extension of the coherent emission of infra-red lasers to shorter wavelengths in the visible and near ultraviolet. However, the demand for low-cost and full compatibility with on-chip integration poses serious constraints to the implementation of realistic devices, which must satisfy the requirement of low energy consumption and, possibly, continuous-wave operation.

Several types of optical nonlinear effects are actively being explored to realize a variety of integrated signal-processing devices on micro- and sub-micrometric scales, including for example four-wave mixing (FWM) [2, 3, 8, 9], self-phase modulation (SPM) [10–12], stimulated Raman scattering (SRS) [4, 13–15] and third-harmonic (TH) generation [16]. A breakthrough example is the demonstration of a continuous-wave silicon Raman laser in the telecom band [4]. Among others, field-confining structures based on silicon photonic crystals (PhC), such as linear waveguides [17–19] or defect nanocavities [20, 21], offer new strategies for improving nonlinear optical efficiency by a unique combination of strong local-field enhancement and light dispersion engineering [22–24]. Visible light emission in silicon through slow-light enhanced third-harmonic generation has been reported very recently [16] in PhC waveguides with only few watts of peak power. This demonstrates the potential of a PhC-based platform for applications involving efficient nonlinear frequency conversion, such as the extension of infrared laser sources to the visible and near ultraviolet windows. However, the implementation of such optically pumped structures in realistic integrated devices faces a number of cost-related obstacles, and it is clearly incompatible with expensive high-power pulsed lasers. For practical

applications, continuous-wave (CW) frequency conversion by means of simple, low-power and low-cost infrared sources such as semiconductor laser diodes would be highly desirable.

In this work, we demonstrate experimentally and analyze theoretically a low-power, continuous-wave and multi-color light source on a silicon chip by simultaneous second- and third-harmonic generation. The visible nano-emitter is a high-Q silicon PhC nanocavity optically coupled to a low-power telecom laser, giving rise to dual-wavelength nonlinear conversion with only few microwatts of CW infrared power. This is made possible by a combination of ultra-small modal volume and engineered near- and far-field profiles of the PhC cavity, which allow to vertically pump and collect the harmonic signals. The results show the great potential of properly optimized nanoscale photonic crystal cavities to enhance nonlinear optical effects even in a material, like silicon, which is not commonly employed for nonlinear optics. Perspectives for applications in other geometries are discussed later in this work.

2. Cavity-enhanced harmonic generation

Frequency conversion by harmonics generation (HG) is derived from the nonlinear susceptibility of a material [6, 7]. In general, this nonlinear optical process involves the conversion of a number n of photons at a fundamental frequency ω into one single photon at frequency $n\omega$ through the n -order susceptibility $\chi^{(n)}$. The intensity of the harmonic signal for the n -order conversion process scales as $(I_\omega)^n$, where I_ω is the electric field intensity of the pump beam. In high-Q resonant cavities, this power scaling translates into an intensity of the harmonic signal being proportional to $(Q/V)^n$, where V is the cavity mode volume. Thus, the use of integrated micro- and nano-cavities possessing both high Q-factors and very small modal volumes, of the order of a cubic wavelength, can result in a dramatic enhancement of the nonlinear conversion efficiency. This strategy has been shown to be very effective in integrated devices such as ultrahigh-Q silica microtoroids [5] and III-V-based photonic crystal cavities [25–28], where low-power CW third-harmonic generation (THG) and second-harmonic generation (SHG) have been observed, respectively. In silicon-based systems, however, although a range of other nonlinear processes have been widely reported using low-intensity CW light [2–4], enhanced HG has only been observed under high-power pulsed excitation ($P_{peak} > 10$ W) [29–33]. A main difficulty related to host silicon material is that the bulk second-order susceptibility vanishes in the electric dipole approximation, leaving only weak electric quadrupole and magnetic dipole contributions, as well as surface-related contributions which add to the bulk quadrupole [34–37]. Also, for Si-based devices optically pumped in the telecom bands at $\lambda \sim 1.35$ to $1.55 \mu\text{m}$, both SHG and THG frequencies fall into the visible spectral region, well above the Si absorption-edge at $\lambda = 1.1 \mu\text{m}$, and are therefore strongly absorbed. Moreover, free-carrier absorption induced by two-photon absorption (TPA), which is considerable in silicon with a TPA coefficient $\beta = 0.5 \text{ cm/GW}$ [38], enables a strong competing channel that further reduces HG efficiency. These material limitations become even more important for high-Q resonators based on totally-guided propagating optical modes, such as integrated silicon micro-rings or micro-disks, where the emitted HG light remains trapped in the device by total internal reflection and is therein quickly absorbed. Also, the relatively long free-carrier lifetime ($\tau \sim 1 - 10$ ns) reported for these systems [3] has been shown to strongly increase TPA induced losses, such as, e.g., in silicon Raman lasers [38].

Our approach, based on planar PhC nanocavities, overcomes these difficulties and allows us to observe efficient CW generation of frequency harmonics in silicon by exploiting (i) the huge nonlinear enhancement due to extreme field localization, leading to an increased efficiency by a factor $Q/V \sim 10^5/\mu\text{m}^3$; (ii) an optimized far-field profile of the PhC cavity, which allows the improvement of the in-coupling efficiency of the pump beam by more than an order of magnitude with respect to conventional high-Q PhC cavities; (iii) the high surface-to-volume

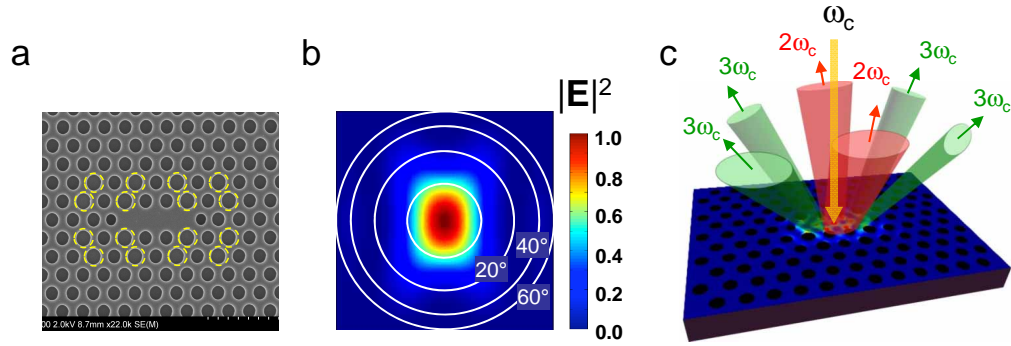


Fig. 1. The system under consideration. (a) SEM image of the fabricated device; the enlarged holes around the cavity are marked in yellow. (b) Far-field intensity profile calculated for the cavity shown in (a) by 3D FDTD simulation. (c) Sketch of the SHG and THG emission from our PhC cavity.

ratio given by the PhC background lattice, which limits the absorption of the HG light through a reduced free-carrier lifetime ($\tau \sim 100$ ps) [39].

3. Fabrication and measurements

Our nonlinear emitter is a modified L3 PhC nanocavity in a 220 nm thick air-suspended silicon membrane, optimized for best Q-factor and in-coupling efficiency at $\lambda_c \sim 1.35 - 1.55$ μm , where λ_c is the cavity resonant wavelength. The device was fabricated from a SOITEC silicon-on-insulator wafer using electron-beam lithography with a hybrid ZEISS GEMINI 1530/RAITH ELPHY system and reactive ion etching with a CHF₃/SF₆ gas mixture. The lattice constant of the photonic crystal was 420nm with $r/a = 0.28$. Further details on device fabrication have been previously reported [19,40]. A scanning electron microscope (SEM) image of a typical device is shown in Fig. 1a. The modified holes around the cavity, slightly enlarged with respect to the background PhC lattice, increase the in-coupling efficiency of the pump beam, which is focused onto the nanocavity from the top (see schematic picture in Fig. 1c). This is achieved through a suitable folding of the k-vector components [41–43] at the resonance frequency $\omega = \omega_c = 2\pi c/\lambda_c$ into the radiative light cone. The resulting far-field profile (Fig. 1b) calculated by 3D finite-difference time domain (FDTD) simulation [44] is nearly Gaussian-like and ensures that sufficient power from the normally incident pump is transferred to the cavity mode, and then converted into HG light emission (Fig. 1c). Further details on our cavity designs, optimized for both high-Q [45,46] and high coupling efficiency [43], have been previously reported.

The modified PhC nanocavities were optically characterized by means of resonant light scattering (RS) spectroscopy [47, 48]. This allowed the determination of their resonance wavelength, quality factor and coupling efficiency to the infrared laser pump, as in our previous report [43]. The measured RS spectra, as those shown in Fig. 2a,b (left panels), are fitted with a Lorentzian or a Fano lineshape [48] to extract the precise resonance wavelength λ_c and Q-factor of the cavity mode. Furthermore, the coupling efficiency of the exciting laser beam is estimated by the ratio of the RS intensity (peak height) to the incident light intensity as [28] $\eta_{cav} = I_{RS}/I_{inc}$. Although the Q-factor of the modified cavity is decreased as compared to the unmodified one, a good compromise is found in our case for cavities having a coupling efficiency of the order of $\eta_{cav} \sim 0.05 - 0.15$ and corresponding Q-factors varying from 5.8×10^4

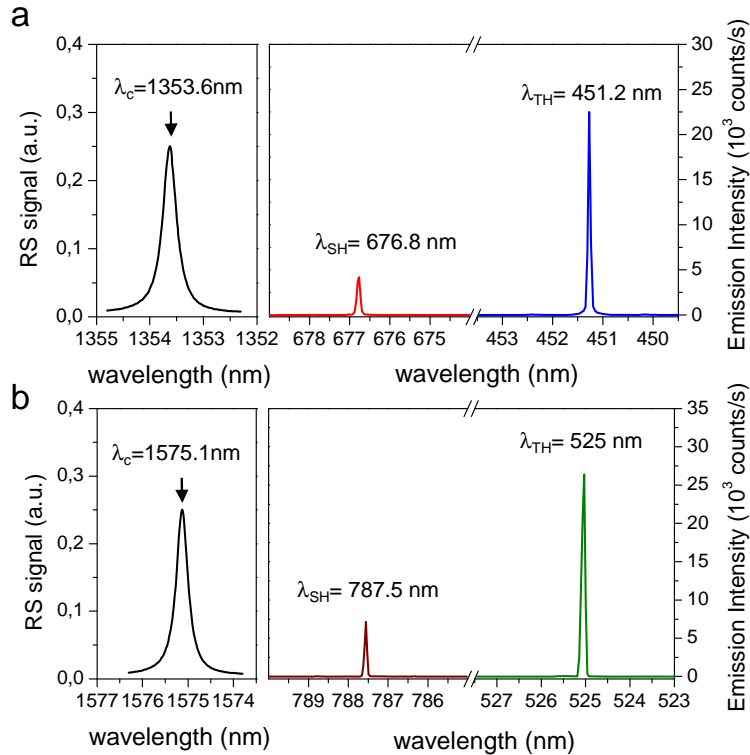


Fig. 2. Experimental demonstration of simultaneous SHG and THG. (a) Resonant scattering spectrum (left) of a PhC nanocavity with fundamental mode at $\lambda_c = 1353.6$ nm (pump wavelength). SHG and THG emission spectra (right) at red and blue wavelengths $\lambda_{SH} = 676.8$ nm and $\lambda_{TH} = 451.2$ nm, respectively. (b) Resonant scattering spectrum (left) of a PhC nanocavity with fundamental mode at $\lambda_c = 1575.1$ nm (pump wavelength). SHG and THG emission spectra (right) at deep-red and green wavelengths $\lambda_{SH} = 787.5$ nm and $\lambda_{TH} = 525$ nm, respectively.

to 1.8×10^4 , as also shown later in Fig. 5a.

When pumping a modified PhC nanocavity with a 1 mW (~ 0.15 mW coupled power) infrared laser tuned to resonance with the fundamental mode at $\omega = \omega_c$, a bright visible emission at $\omega = 3\omega_c$ (THG) and a less intense one at $\omega = 2\omega_c$ (SHG) are simultaneously observed. We tested different PhC cavities having fundamental resonant wavelengths λ_c in the range from 1350 nm to 1580 nm, which gave THG emission tuned in the blue/green visible window (450 - 525 nm) and SHG in the red (675 - 790 nm), as shown in Fig. 2. The continuous-wave SHG and THG of the devices were probed using the same experimental set-up used for RS characterization, in which the crossed polarizers have been removed and the beamsplitter replaced by a dichroic mirror. The low-power pump beam from the 1350-1640 nm tuneable laser was tuned to resonance with the cavity mode and focused on the sample from the top by means of a 50x microscope objective with NA=0.8. Visible SH and TH emission were collected through the same objective and then dispersed by a 500 mm focal length monochromator equipped with a liquid Nitrogen cooled Si CCD (Princeton Instruments). Typical SH and TH emission spectra from a "blue" cavity and a "green" cavity are shown in Fig. 2a,b (right panels), respectively. Notice that SH and TH spectra are not resolved. To measure the total SH and TH emission

power and to verify their scaling behavior as a function of the pump power, the entrance slit of the monochromator was fully opened to assure that the whole HG emission pattern was collected by the Si CCD. Linearity and power response of the Si CCD was calibrated using a doubled Nd:YAG laser monitored by a power meter.

4. SHG and THG radiation patterns

Due to its centro-symmetric nature, bulk crystalline Silicon has a third-order nonlinear susceptibility tensor but no bulk electric dipole second-order susceptibility. However, SHG is possible in Silicon as a surface contribution, which adds to the weak bulk quadrupole and magnetic dipole contributions [6, 7, 34–36]. The bulk contribution is measurable but small [29, 37] and it will be neglected in the following. We model these two different contributions with 3D FDTD simulations of the electric field generated from suitably determined nonlinear polarizations, following a procedure similar to the one already employed in Ref. [25]. Absorption at the respective harmonic frequencies is taken into account through the complex refractive index of Silicon.

Notice that, since we are considering HG from localized cavity modes, there is no propagating field within the nonlinear material and the usual conditions of phase matching in propagation cannot be applied. Full phase matching in a cavity geometry requires simultaneous resonance at the pump and harmonic frequencies, as well as spatial overlap of the field profiles. In the present case, double resonance cannot be achieved since the field at the harmonic frequency is strongly absorbed in the cavity medium for both SHG and THG. Therefore, phase matching considerations are not an issue in the present experiments.

In Fig. 3a,b we plot the calculated near-field profiles of the electric field at $\omega = \omega_c$, decomposed in the two orthogonal components E_x and E_y . Unlike in Si microrings or nanowire waveguides, here the electromagnetic field is strongly localized in a tiny volume inside the cavity with a peculiar spatial distribution: while E_y sharply peaks at the center of the cavity region, i.e. in the bulk of the Si membrane, E_x shows eight intense relative maxima located just at the border of the holes surrounding the PhC cavity. This unique feature given by the PhC lattice leads to a strong nonlinear interaction involving both surface-related (SHG) and bulk-related (THG) contributions to the nonlinear susceptibility at the same time.

The TH nonlinear polarization is calculated as [37]

$$P_{x,y}(3\omega_c) = 3\chi_{1212}^{(3)}|\mathbf{E}(\omega_c)|^2 E_{x,y}(\omega_c), \quad (1)$$

where $\chi_{1212}^{(3)}$ is the third-order nonlinear susceptibility. In Eq. 1 we have neglected the small nonspherical terms. The nonlinear TH polarization components depend on the field profiles shown in Fig. 3a,b. We assume a discrete set of dipoles oscillating at frequency $3\omega_c$ to be placed in the relative maxima of $\mathbf{P}(3\omega_c)$: five y-polarized dipoles are placed along the cavity axis, while eight x-polarized dipoles are placed off-axis close to the PhC holes around the cavity. The amplitudes of the dipoles are proportional to the local values of the nonlinear polarization and a phase of π is given to dipoles placed in the relative maxima with opposite signs. The generated near-field is recorded just above the PhC cavity surface and then propagated with a near-to-far field transformation using the FDTD method.

The SHG is modeled along the same lines, but the nonlinear interaction in the centrosymmetric silicon material is now dominated by the surface effects. The second-order nonlinear polarization is determined by the surface contribution at the Silicon-hole boundaries. The field maxima in Fig. 3a occur at the positions of the eight holes close to the cavity and the electric field at the maxima is along the x direction. Modelling the second-order surface nonlinear tensor in the approximation of an isotropic vertical sidewall surface [6], the nonlinear polarization

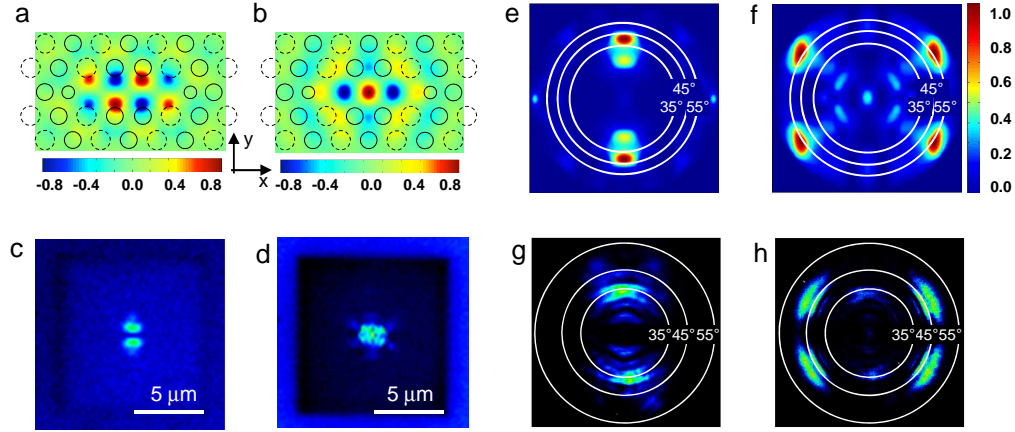


Fig. 3. SH and TH near- and far-field emission. (a),(b) E_x and E_y components of the calculated electric field inside the PhC cavity at the resonance frequency. (c),(d) Spectrally filtered optical image of the SHG and THG emission taken with a high sensitivity Si CCD, respectively. (e),(f) Corresponding experimental Fourier images (see methods) showing the polar far-field emission profile of the SHG and THG light. (g),(h) Calculated far-field patterns (see methods).

is found to be along the y direction and it is given by (notice that the normal to the surface is along y):

$$P_y(2\omega_c) = \chi_{311}^{(2)} E_x^2(\omega_c). \quad (2)$$

Considering the second-order nonlinear tensor components for the microscopic symmetry of the surface [37], for a cavity axis along the [110] direction of the cubic silicon lattice, yields the same result since the electric field is dominated by the x component. In practice, the nonlinear polarization is modeled by eight dipoles in the positions indicated by the field maxima in Fig. 3a, oriented along the y direction.

In this description of the second-harmonic generation process, the overall symmetry properties of the system are preserved: the cavity structure is symmetric under mirror reflection in the xz plane and the fundamental cavity mode, which is odd under mirror reflection (notice the parities of the E_x and E_y components in Fig. 3a,b), is indeed excited by an incident e.m. wave polarized along y . The nonlinear dipoles, whose phases are determined by the electric field distributions in Fig. 3a,b, are also odd under mirror reflection in the xz plane. The interference between the fields produced by the nonlinear dipoles is essential in determining the far-field profiles of the second-harmonic, to be shown below.

The spatial regions within the PhC cavity giving rise to these two contributions can be experimentally identified by taking the optical images of the emitting cavity selectively filtered at the THG and SHG wavelengths, as shown in Fig. 3c,d, respectively. Pictures are obtained by using a 50x NA=0.8 microscope objective in combination with a f=400 mm tube lens, to realize a 100x magnified image of the PhC cavity and emission pattern on the liquid Nitrogen cooled Si CCD. We see that the THG image shows up all of the intensity maxima corresponding to the sum of both $|E_y|^2$ and $|E_x|^2$ contributions to the electric field. On the other hand, the SHG image is characterized by two bright lobes separated by a dark region just at the cavity location, indicating that only the E_x component is contributing to SHG emission and confirming its surface-related nature.

The SHG and THG far-field radiation patterns of the PhC nanocavity, i.e. the polar emission

profiles, were then measured experimentally using a Fourier-imaging technique. This consists in performing the optical Fourier-transform of the light emitted at the sample surface by means of an additional lens placed between the objective and the Si CCD. An image of the back-focus of the objective lens is thus created directly on the Si CCD, which represents the far-field radiation pattern of the PhC nanocavity. The Fourier images of the SHG and THG light, selectively filtered at the respective wavelengths, are shown in Fig. 3e,f. For comparison, the calculated far-fields at SH and TH frequencies are shown in Figs. 3g,h, which agree fairly well with the measured patterns. In particular, the four-lobes TH and the double-lobe SH far-field emissions are nicely reproduced within the model. Most importantly, we can confirm that THG is a bulk effect, as opposed to SHG which originates from surface contributions at the vertical hole sidewalls. It will be interesting for future work to investigate the dependence of SH and TH signals on pump beam polarization, as this may provide additional information, e.g., on surface vs. bulk contributions for SHG and on cavity mode symmetries.

5. Scaling behavior

The effects we demonstrate here are second-order (SHG) and third-order (THG) nonlinear processes in an optical nanocavity, which are expected to show a square and a cubic dependence on the pump power at the resonance wavelength, respectively. In Fig. 4a we report a log-log plot of the emitted SHG and THG signals versus the coupled pump power for a PhC nanocavity having the fundamental mode at $\lambda_c = 1578$ nm and quality factor $Q = 5.2 \times 10^3$. For low-power excitation, i.e. for coupled powers < 100 μ W, both the SHG and THG emission closely follow the predicted scaling behavior. However, at higher coupled power a slight saturation sets-in due to free-carrier absorption induced by TPA, which come into play upon increasing the electromagnetic energy stored inside the cavity. As a result, a reduction in the conversion efficiency is observed due to i) thermo-optic effect and ii) degradation of the cavity Q-factor. The first effect causes thermal heating of the PhC cavity and induces a red-shift of the cavity mode [49, 50]. Then, the de-tuning of the resonance wavelength with respect to the pump beam leads to a reduced coupled power and a reduced HG efficiency. On the other hand, the significant free-carrier absorption at the pump frequency degrades the Q-factor of the cavity and, once again, reduces the HG efficiency. Moreover, strong free-carrier absorption also occurs at the SH and TH frequencies, further reducing the conversion efficiency.

By increasing the quality factor of the PhC cavity, a strong increase of HG conversion efficiency is expected according to the scaling as $(Q/V)^n$. However, the detrimental effects of TPA are also expected to increase significantly as the Q rises [50]. In Fig. 4b we report the power dependence of SHG and THG for a PhC cavity with a quality factor $Q = 3.2 \times 10^4$. A much higher nonlinear emission than in the low- Q cavity is observed, with a maximum output power of ~ 0.05 pW at the SH and ~ 2 pW at the TH frequencies, for 100 μ W coupled power. On the other hand, a pronounced saturation due to the degradation of the cavity Q-factor is clearly evident even at low coupled powers. The saturation occurs at similar output powers, meaning that the increased Q-factor reduces the pump power required. The occurrence of a red-shift of the cavity mode indicates that the cavity is entering an optical bistable regime due to a temperature-induced nonlinear variation of the cavity refractive index [49, 50]. In our experiment, in order to compensate for this thermo-optic effect, the pump wavelength is varied along with the pump power to track the red-shift of the cavity resonance.

The overall efficiency of cavity-enhanced HG processes critically depends on both coupling efficiency and Q-factor at the resonant pump wavelength. Figure 5a (upper panel) shows the Q-factors of the far-field optimized PhC cavities and the corresponding coupling efficiency, as a function of the radius of the modified holes, Δr (see Fig. 1a). Assuming that the mode volume of each PhC cavity remains almost unchanged, we expect the HG signal to scale as $(Q\eta_{cav})^2$ for

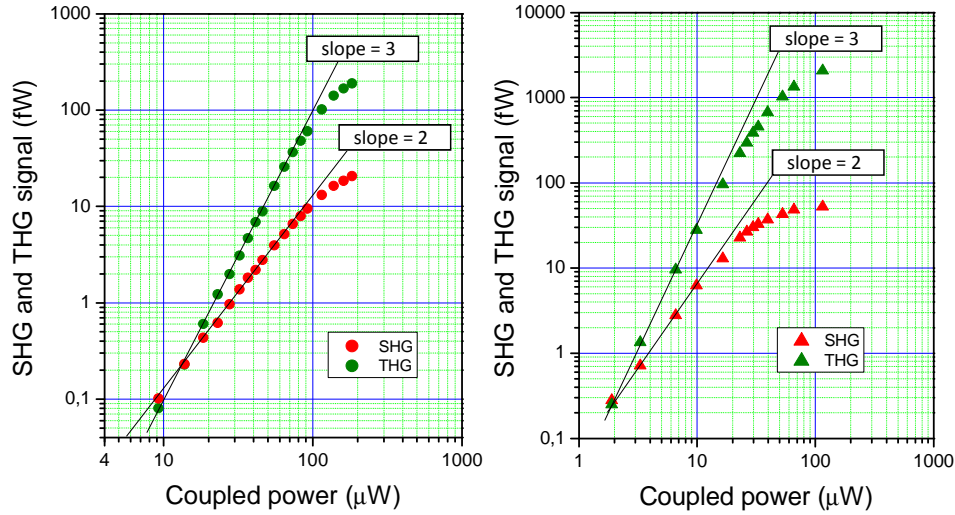


Fig. 4. Power scaling and conversion efficiency. (a) SHG and THG emission intensity versus coupled pump power for a PhC nanocavity with coupling efficiency 0.2 and quality factor $Q = 5.2 \times 10^3$, at fixed pump wavelength. (b) SHG and THG emission intensity versus coupled pump power for a PhC nanocavity with coupling efficiency 0.12 and quality factor $Q = 3.2 \times 10^4$. Pump wavelength has been varied for increasing pump power to account for thermo-optical induced red-shift of the cavity mode.

the SH process and as $(Q\eta_{cav})^3$ for the TH one. In the lower panel of Fig. 5a, the product $Q\eta_{cav}$ is explicitly shown. Indeed, such a scaling is experimentally verified in Fig. 5b, where maximal SHG and THG signals are observed for the far-field optimized PhC cavity with $\Delta r = 6$ nm, which shows the highest value of $Q\eta_{cav}$ (see Fig. 5a, lower panel). Then, very clear Q^2 and Q^3 scaling behaviors for the SHG and THG processes are obtained by normalizing the measured signals from each cavity by η_{cav}^2 and η_{cav}^3 , respectively (Fig. 5c). To further confirm the SH and TH scaling behavior as a function of the optical power coupled to the PhC cavity, we report in Fig. 5d the measured SHG and THG intensity recorded as the pump laser is scanned across the cavity resonance. The resonant scattering spectrum of the cavity mode is also reported with a best-fit to a Lorentzian lineshape. We see that the SHG and THG spectra are very well described by the squared and cubed Lorentzian lineshape used to fit the fundamental resonance. These observations represent definite proof that our results should be interpreted as cavity-enhanced nonlinear frequency conversion by SHG and THG. From the above, it is clear that the HG conversion is not a parametric process, i.e. a resonant mode at the converted frequency is not required.

The maximum conversion efficiency observed in our PhC device, defined as $\eta = P_{out} / P_{in}$, can be evaluated for SHG and THG from the plots of Fig. 4a,b. We estimate $\eta_{SH} \sim 1 \times 10^{-9}$ for the SHG process and $\eta_{TH} \sim 2 \times 10^{-8}$ for the THG one. However, since we are dealing with CW conversion efficiencies, a more appropriate comparison with previously reported results is obtained by evaluating the normalized conversion efficiencies as $\rho_{SH} = P_{out} / P_{in}^2$ for the SHG process and $\rho_{TH} = P_{out} / P_{in}^3$ for THG one. This yields $\rho_{SH} \sim 3 \times 10^{-5} / W$ and $\rho_{TH} \sim 8 / W^2$, respectively. For comparison, the normalized SH conversion efficiency for a focusing area of $\sim 1 \mu m^2$ is of the order of $10^{-14} / W$ in bulk silicon [29] and it is enhanced by no more than 2-3 orders of magnitude in microcavities and 2D photonic crystals [30–33]. For THG, the highest reported normalized conversion efficiency is $10^{-10} / W^2$ [16]. Thus, by using silicon PhC

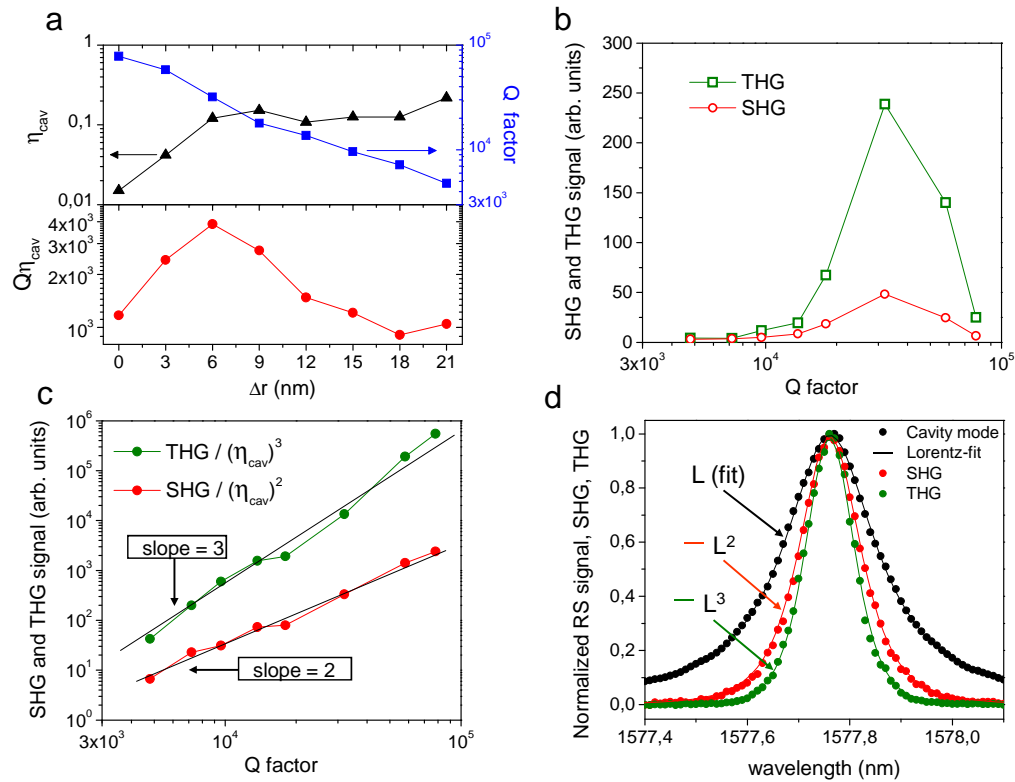


Fig. 5. Q-factor and lineshape scalings. (a) Upper panel, Q-factor (right axis) and corresponding coupling efficiency η_{cav} (left axis) of the far-field modified PhC nanocavities as a function of the holes enlargement Δr . Lower panel, the product $Q\eta_{cav}$. (b) SHG and THG emission intensity vs. Q-factor for the same series of PhC cavities. The HG signals peak around $Q \sim 3 \times 10^4$, which corresponds to the cavity with $\Delta r = 6$ nm in (a) that has the highest $Q\eta_{cav}$ product. (c) Normalized SHG and THG emission intensity (see text) as a function of the cavity Q factor showing clear Q^2 and Q^3 scaling, respectively. (d) Resonant scattering spectrum of a PhC nanocavity with $Q = 5.2 \times 10^3$ (black dots), and best-fit to a Lorentzian lineshape (black line, L). SHG and THG spectra recorded while scanning the pump laser across the cavity resonance (red and green dots, respectively). Red and green lines interpolating the SHG and THG data are the squared (L^2) and cubed (L^3) Lorentzians, respectively.

nanocavities to enhance optical nonlinearities, we demonstrate an impressive improvement in THG efficiency of more than 10 orders of magnitude and a reduction in pump power by 6 orders of magnitude.

6. Discussion and conclusions

Despite the onset of saturation in the HG signal occurring for high-Q PhC cavities, our experiments represent a considerable improvement over previous works on silicon [30–33], since HG light is observed here under a continuous-wave pumping regime. This is quite unexpected due to the presence of strong TPA and consequent free-carrier absorption in silicon - the same parasitic effect that prevents cw Raman lasing in Si devices unless a free-carrier lifetime reduction mechanism is applied [15]. We demonstrate here that efficient continuous-wave HG is possible in a silicon nanodevice, thus making the major step towards possible widespread applications. Moreover, we note that the pump power required to observe efficient emission is ten times lower than that for a recently demonstrated microlaser [51], which highlights the surprising fact that light sources based on HG emission may be more efficient than lasers.

Even though at present the maximum observed THG power may be considered still low for immediate applications in signal processing devices, the conversion efficiency of our device can be further increased in several ways: 1) by increasing the $Q\eta_{cav}$ product, i.e. by designing PhC nanocavities with higher Q-factor and coupling efficiency, while keeping a comparable mode volume; 2) through polarization of the device with a p-n junction to sweep-out free-carriers from the cavity region, i.e. as in Raman laser devices [15]; 3) by the introduction of carrier-recombination centers through controlled ion-implantation [52]. The combined application of these strategies is expected to increase substantially the emission efficiency by 2-3 orders of magnitude, thus bringing the blue-THG output power of our Si nanocavity to a level that is comparable to the highest reported (~ 500 pW) red-SHG power in a III-V-based nanodevice [28].

In the present geometry the pump electromagnetic field is in-coupled through far-field optimization out of the plane. We point out that an alternative integrated signal-processing device could be realized by pumping the cavity through a side-coupled PhC waveguide in a geometrical configuration already reported [20]. This would lead, for instance, to a channel-drop device where infrared signals could be injected on-chip and "dropped" out-of-plane at visible wavelengths. On the other hand, achieving a full on-chip device for both pump and harmonic signals would require to suppress absorption, i.e., to change the PhC slab material in order to have transparency also at the harmonic frequency.

In conclusion, we have presented the first demonstration of nonlinear frequency conversion by simultaneous SHG and THG in silicon PhC nanocavities using low-power continuous-wave light. We achieved efficient dual wavelength emission in the blue/green and red visible windows with excitation in the telecom bands and with a few tens of microwatts power. The low-power continuous-wave operation, wide tunability and full CMOS compatibility of our silicon nanodevice are important features which add considerable weight to the opportunity of making silicon a truly pervasive material for Photonics.

Acknowledgments

The authors would like to acknowledge D. Bajoni and M. Liscidini for useful discussions and S. L. Portalupi, M. Spurny, S. Balfour and G. Robb for help with experiments. This work was partly supported by Era-NET NanoSci LECSIN project coordinated by F. Priolo, and by Italian Ministry of University and Research, FIRB contract no. RBAP06L4S5. Fabrication was carried out in the framework of NanoPIX (www.nanophotonics.eu).